

Development and Assessment of Deployed Sensors and Technologies Supporting Molten Salt Loop Operations

Chemical and Fuel Cycle Technologies Division

About Argonne National Laboratory

Argonne is a U.S. Department of Energy laboratory managed by UChicago Argonne, LLC under contract DE-AC02-06CH11357. The Laboratory's main facility is outside Chicago, at 9700 South Cass Avenue, Argonne, Illinois 60439. For information about Argonne and its pioneering science and technology programs, see www.anl.gov.

Disclaimer

This report was prepared as an account of work sponsored by an agency of the United States Government. Neither the United States Government nor any agency thereof, nor UChicago Argonne, LLC, nor any of their employees or officers, makes any warranty, express or implied, or assumes any legal liability or responsibility for the accuracy, completeness, or usefulness of any information, apparatus, product, or process disclosed, or represents that its use would not infringe privately owned rights. Reference herein to any specific commercial product, process, or service by trade name, trademark, manufacturer, or otherwise, does not necessarily constitute or imply its endorsement, recommendation, or favoring by the United States Government or any agency thereof. The views and opinions of document authors expressed herein do not necessarily state or reflect those of the United States Government or any agency thereof, Argonne National Laboratory, or UChicago Argonne, LLC.

Development and Assessment of Deployed Sensors and Technologies to Support Molten Salt Loop Operations

prepared by
Nora A. Shaheen
Jicheng Guo
Nathaniel C. Hoyt
Chemical and Fuel Cycle Technologies Division, Argonne National Laboratory

September 30, 2024

Acknowledgements

This report has been submitted in fulfillment of Milestone RD-24AN060203 (*Complete Development of Automated Sensor and Corrosion Control System for Deployment to Molten Salt Loops*) and M3AT-24AN0702031 (*Design, Purchasing, and Preparation for Installation of Actinide Loop*). It was produced under the auspices of the US DOE Office of Nuclear Energy's MSR Campaign, Dr. P. Paviet National Technical Director and Michael Stoddard Federal Manager.

This work was conducted at Argonne National Laboratory and supported by the U.S. Department of Energy, Office of Nuclear Energy, under Contract DE-AC02-06CH11357.

Thanks to Kevin Robb at Oak Ridge National Laboratory for providing support related to sensor testing within the FASTR molten salt loop.

Abstract

During FY24, Argonne conducted a variety of activities to develop and assess new monitoring and control technologies towards enabling long-duration operations of molten salt reactor systems. The first objective of the work completed this year was to deploy technologies capable of reliably and rapidly monitoring the operational health of a molten salt loop. To achieve this, the project focused on specific tasks, including: (1) electroanalytical technique development for use in deployed sensors, and (2) operations of sensors on the Facility to Alleviate Salt Technology Risks (FASTR) loop at Oak Ridge National Laboratory. The second objective of the work this year focused on creating a pumped actinide flow loop to enable long-duration salt chemistry and corrosion studies using uranium-bearing fuel salts. Toward that end, we designed and procured a loop capable of being installed into a radiological glovebox at Argonne. A corrosion control system was also designed for integration into this loop. These combined systems will enable the feasibility of corrosion control and management systems to be investigated with complex chloride fuel salt mixtures.

1. Introduction

Corrosion monitoring, mitigation, and control are essential for minimizing safety hazards and ensuring the long-term operation of molten salt reactors (MSRs). While several potential corrosion pathways exist in MSRs, exogenous impurities introduced into the salt are of particular concern as well as long-term redox changes resulting from the generation of fission products.^{1,2} Oxide species are the primary exogenous impurity and may be introduced through selective dissolution of structural components' passive layers, atmospheric ingressions as a result of leaks, or through insufficient salt purification.³ The presence of oxides may initiate a sequence of operational issues that further promote the acceleration of corrosion mechanisms. As such, careful monitoring and control of impurities such as oxides is critical to enable the long-term operation of MSRs. To address these issues, our objectives this year included: (1) the development of new methodologies and capabilities for monitoring the chemistry within molten salt flow loops, (2) deployment and testing of sensors to monitor operational loops as part of the MSR Campaign, (3) finalization of a deployable corrosion control system design, and (4) the design and the procurement of an actinide loop that can be installed into a radiological glovebox.

The sensor development work this year focused on the creation of improved electroanalytical approaches capable of rapidly monitoring species within molten salt loops across a full range of concentrations. These efforts targeted the early detection of low-concentration (~1 ppm) impurities along with measurements up to very large concentrations (>100,000 ppm). Capturing this full span will help to ensure that such corrosion control mechanisms can be initiated rapidly upon the detection of impurities while ensuring that large concentrations are appropriately quantified if additional control measures must be taken. Measurements across low and high concentrations, however, require special methodologies as nonideal behavior (e.g. effects from finite ionic conductivities) can distort traditional measurements. These contributions may attenuate data such that sensors deployed in molten salt loops unpredictably under- or overestimate salt conditions. By coupling numerical simulations with experiments, we were able to quantitatively correct for these attenuations in potential pulse and sweep techniques in a model system. This approach was then applied to build on work completed in FY23 and study the behavior of O^{2-} in molten FLiNaK at various temperatures to deduce temperature-dependent properties.

We also deployed salt monitoring tools at a molten salt loop operated by MSR Campaign collaborators. Specifically, sensors were deployed in the Facility to Alleviate Salt Technology Risks (FASTR) loop at Oak Ridge National Laboratory. We also constructed a new Littlewood diagram to predict chemical speciation within the FASTR loop's salt using fundamental thermodynamic information. The combined experimental observations and Littlewood diagram allowed us to determine the ideal operational envelope of the loop to support long-term operations.

Finally, the design and procurement of components necessary to build a pumped actinide loop and corrosion control system was begun. The loop will operate inside a radiological glovebox that is capable of maintaining an inert atmosphere. To determine the operational integrity of the salt, we will install electrochemical sensors at various points on the loop. These combined technologies will be used to inform the use of a corrosion control system that will also be deployed within the loop.

2. Sensor development

In developing sensor technologies for use in molten salt media, it is important to ensure the sensors are properly calibrated to account for uncompensated ohmic resistance.⁴ We have previously reported the extent to which uncompensated ohmic resistance can generate error in measurements, particularly with pulse techniques such as square wave voltammetry.⁵ This FY, we sought to establish a more robust framework for correcting uncompensated resistance for other contaminant species such as chromium halides, other relevant molten salts, and various operational temperatures. We also extended this analysis to other electroanalytical techniques, namely, linear sweep voltammetry.

The work this year builds on our earlier efforts. For example, in FY23, we reported on the operational state of the Liquid Salt Test Loop (LSTL) at Oak Ridge.⁵ From the sensors deployed in the loop, we measured impurities including hydroxides and identified that the status of the LSTL salt fell outside its ideal operational window. However, measurement and characterization of fundamental properties of soluble oxide ions in molten FLiNaK remained incomplete as the electroanalytical techniques needed to make these measurements were inadequate.

As such, this year we continued our studies in analyzing oxides in molten fluoride salts and developed the capabilities to measure species' concentration across wide ranges. To aid in development of these approaches, we first examined the model redox reaction:



This single-electron soluble-soluble half-reaction shares similarities to the electrochemical reaction that is used to measure oxide, but its redox potential and lack of gas evolution make it a simpler test system. After developing the experimental techniques and digital modeling approaches with respect to this model system, examination of the oxide half-reaction (Equation 2) could then occur via controlled, at-temperature additions of Li₂O to FLiNaK:



This FY, we focused on square wave voltammetry (SWV) and linear sweep voltammetry (LSV) as representative pulse and sweep techniques, respectively. Specific to SWV, variables of particular interest to our discussion for both the CrCl₂ studies in molten chlorides and the O²⁻ studies in molten FLiNaK are the half-width potential ($W_{1/2}$) and the peak current (I_p), given by the following equations for reversible conditions:^{6,7}

$$W_{1/2} = 3.52 \frac{RT}{nF} \quad [3]$$

$$I_p = \frac{nFAD^{1/2}C_b\sqrt{2f}}{\pi^{1/2}}\psi \quad [4]$$

where R is the universal gas constant, T is temperature, n is the number of electrons, F is Faraday's constant, A is the electrode area, D is the diffusion coefficient, C_b is the bulk concentration, ψ is the dimensionless peak current, and f is frequency. In Eq. 3, we note that $W_{1/2}$ is largely independent of various operating conditions, and only a function of number of

electrons transferred and operating temperatures. From Eq. 4, we expect a linear response of peak current with respect to the square root of frequency for a wide variety of frequencies.

Similarly, the variables relevant to LSVs and our discussion are the anodic peak potential (E_p^a), the half-peak potential ($E_{p/2}$), and the anodic peak current (I_p^a). These variables are well established mathematically for reversible conditions through the following relationships:⁸⁻¹⁰

$$E_p^a - E_{p/2} = 2.2 \frac{RT}{nF} \quad [5]$$

$$I_p^a = 0.4463 \left(\frac{F^3}{RT} \right)^{1/2} A n^{3/2} D_{Cr^{2+}}^{1/2} C_b \nu^{1/2} \quad [6]$$

A precise description of the mathematical treatment of the SWV simulations has been previously reported.⁵ LSVs were simulated using an identical methodology, with alterations made only to accommodate differences in the potential-time profile.

2.1. Experimental design

All electrochemical experiments reported in this section were collected in an inert atmosphere glovebox using a three-electrode configuration and a Gamry Interface 5000E potentiostat. Individual components of the molten salts were baked at 450°C for 6 hours to remove residual moisture. The molten chloride (LiCl-KCl) and fluoride salts (FLiNaK) were then homogenized above their respective melting points in boron nitride (binder-free, Grade BN99) crucibles. At-temperature additions of chromium (II) chloride (CrCl₂, 99.99%, added to molten LiCl-KCl) and lithium oxide (Li₂O, 97%, added to molten FLiNaK) were made to collect concentration-dependent measurements. Following each addition, the open circuit was monitored to ensure solution homogenization. Square wave voltammograms were collected at a 12.5 and 2 mV pulse and step potential, respectively, using Gamry’s “Noise Reject” mode.

Simulations used to inform the SWVs and LSVs were conducted using COMSOL Multiphysics® 5.6. To minimize errors introduced by finite element method simulation tools, we used an extremely fine mesh size. The relative tolerance and time steps were maintained at a minimum of 6 orders of magnitude below the simulation run time. The forward and reverse currents were processed in accordance with experimental data processing.

2.2. Results: Sensor Development

2.2.1. Pulse Potential Technique Improvements: Square Wave Voltammetry

Prior to collecting SWVs, cyclic voltammograms (CVs) were taken to identify the electrochemical window wherein the Cr²⁺/Cr³⁺ reaction occurred. Figure 1 shows an example of LSVs collected for 2.4 wt% CrCl₂ in a LiCl-KCl molten salt. Characteristic peaks associated with the Cr²⁺/Cr³⁺ and Cr²⁺/Cr⁰ redox couples were observed. The relative location of these peaks is in good agreement with those reported in literature.¹¹ Moreover, as seen in the inset of Figure 1, the absence of the peaks in the base salt further confirms that these peaks can be attributed to Cr-related redox reactions.

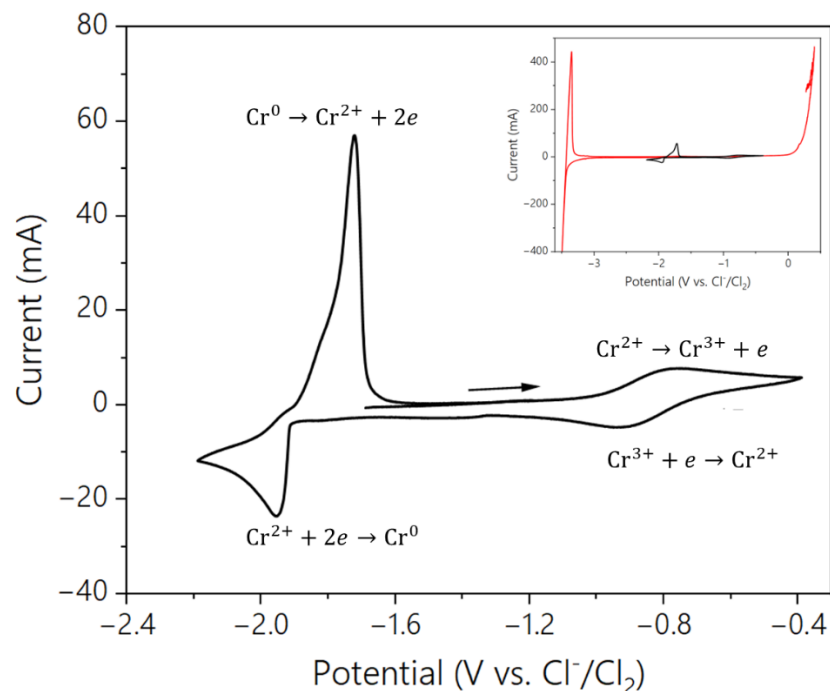


Figure 1. Cyclic voltammogram of (*black*) 2.4 wt% CrCl₂ in LiCl-KCl molten salt collected at 450°C. The inset shows the overlaid CV of CrCl₂ in comparison to the (*red*) base eutectic.

Representative square wave voltammograms are shown in Figure 2a-d. Note that at sufficiently low frequencies (e.g. 20 Hz), the SWV appeared to be symmetrical about the peak potential. However, as the frequency increased, the SWVs became attenuated such that the peak current was dampened and the apparent half-width potential increased. This effect can be seen for a wider range of frequencies in Figure 2e-f. Note in Figure 2e, $W_{1/2}$ increased as a function of frequency, in excess of 500 mV. This is in contrast to predictions from Eq. 3 where the expected $W_{1/2}$ is equal to 220 mV. Additionally, in Figure 2f, the relationship between peak current and square root of frequency was linear only for a small range of frequency and decayed towards zero at sufficiently large frequency ranges.

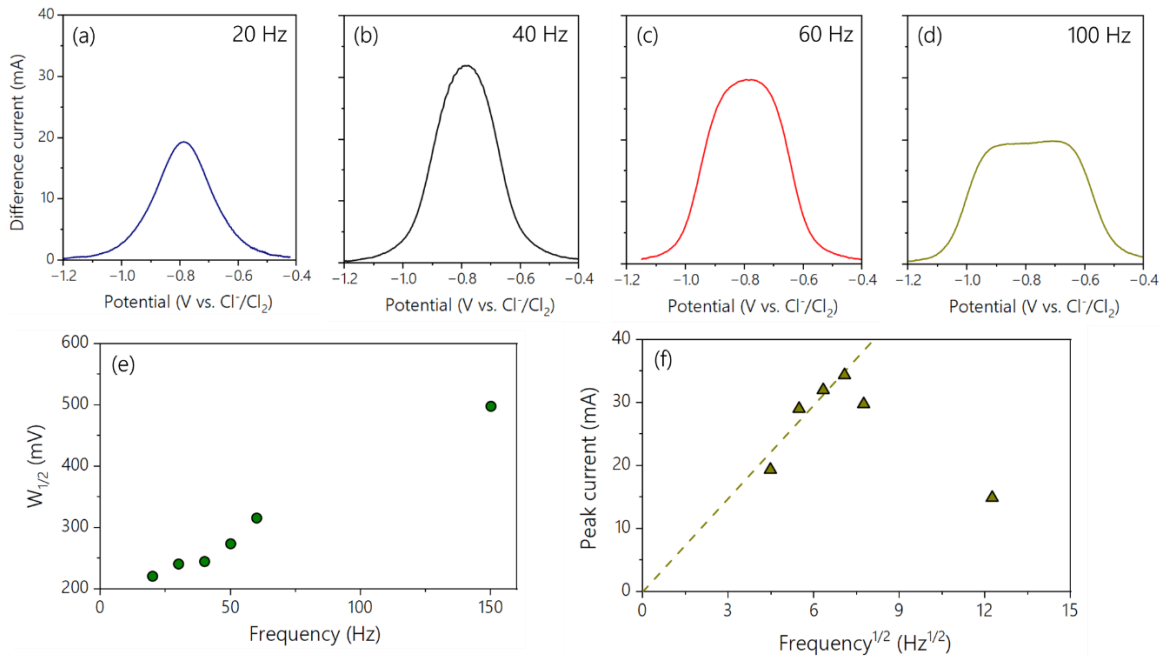


Figure 2. (a-d) Square wave voltammograms collected using 2.2 wt% CrCl₂, (e) the half-width potential versus frequency, and (f) the peak current versus square root of frequency.

This attenuated response has been previously reported in literature for aqueous systems and attributed to uncompensated ohmic resistance.¹² To quantify and ultimately correct this behavior, we simulated SWVs experiencing various amounts of iR_{Ω} at experimentally relevant temperatures, shown in Figure 3a. As reported in FY23, we extracted correction factors (referred to as current multipliers) by relating the simulated peak current density when $R_{\Omega} = 0$ to the peak current density when $R_{\Omega} > 0$:

$$CM = \frac{i_p(R_{\Omega} = 0)}{i_p(R_{\Omega} > 0)} \quad [7]$$

where CM represents current multipliers. Figure 3b shows a graphical representation of the current multiplier and the half-width potential.

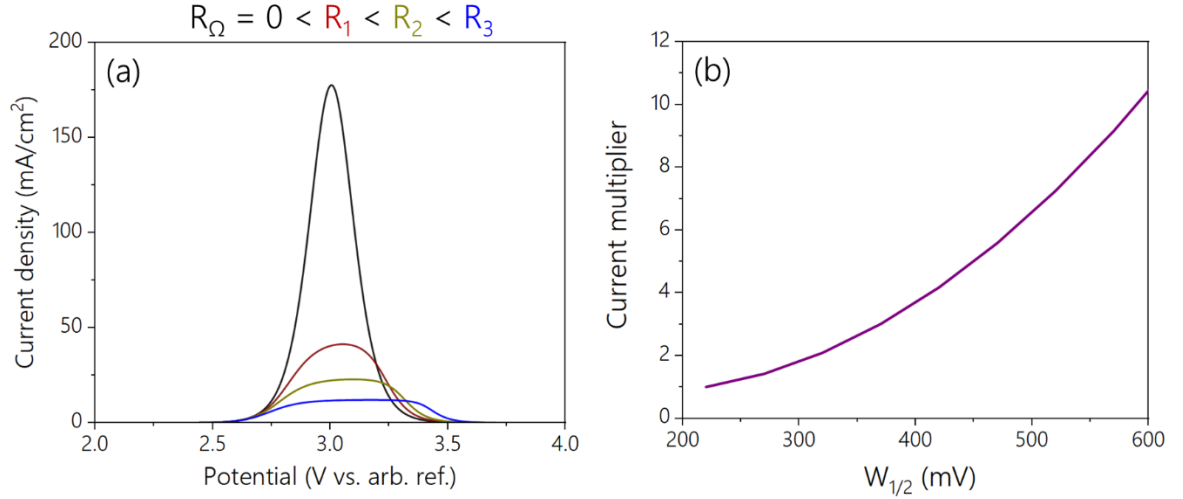


Figure 3. (a) Simulated square wave voltammograms experiencing increasing amounts of ohmic resistance, (b) current multiplier correction factor as a function of half-width potential for single-electron soluble-soluble redox reaction.

Using the correction factor presented in Figure 3b, we can then correct for experimentally observed peak current via the modified Krause-Ramaley equation:⁷

$$I_p^{\text{corrected}} = \frac{nFAD^{\frac{1}{2}}C_b\psi}{\sqrt{\pi}} \sqrt{2f} \times CM \quad [8]$$

Verification that the diffusion coefficient of CrCl_2 in this salt was independent of the CM and SWV approach discussed above was also confirmed to ensure consistency of the models. To do this, we collected LSVs of CrCl_2 using a simplified array structure, the details of which have been reported elsewhere.¹³ A representative set of LSVs collected at various scan rates are shown in Figure 4a, and the corresponding anodic peak current versus the square root of scan rate is shown in Figure 4b. From Figure 4a, we observed that the anodic peak potential was independent of scan rate. This observation, coupled with the linearity of Figure 4b, suggested that the LSVs were fairly reversible at these conditions and the effects of ohmic resistance could be neglected. Note, the latter effect will be discussed in further detail in the proceeding section.

For LSVs involving a soluble-soluble redox transition, the Randles-Sevcik equation can be used to relate the anodic peak current (I_p^a) to scan rate (ν) through the following relationship:

$$I_p^a = 0.4463 \left(\frac{F^3}{RT} \right)^{1/2} A n^{3/2} D_{\text{Cr}_2}^{1/2} C_b \nu^{1/2} \quad [6, \text{revisited}]$$

Using this approach, we calculated $D_{\text{Cr}_2} = 3.95 \times 10^{-6} \text{ cm}^2/\text{s}$ and used it to calculate concentrations in the proceeding discussion.

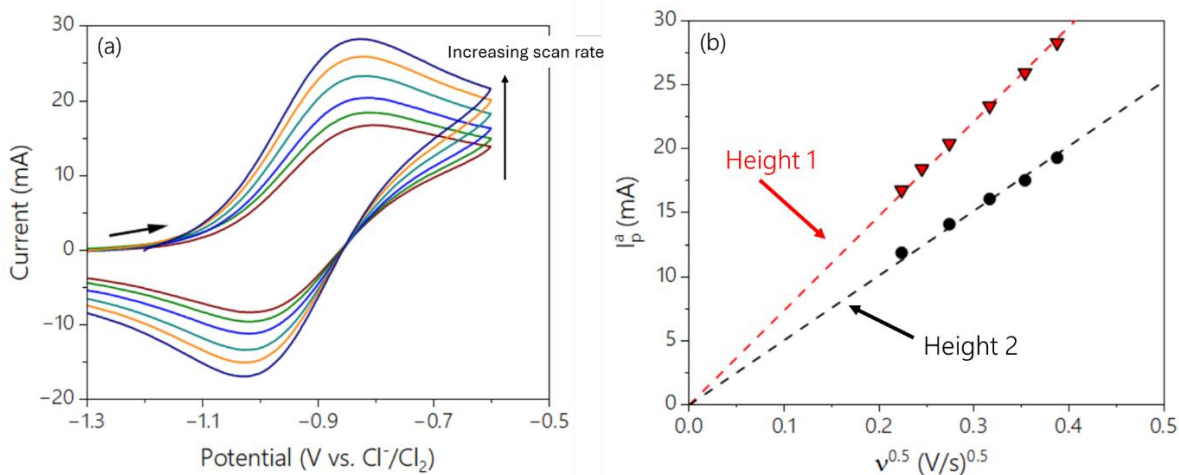


Figure 4. (a) Linear sweep voltammograms collected of CrCl₂ in LiCl-KCl molten salt, and (b) the relationship between anodic peak current and square root of the scan rate.

Using Eq. 4, peak currents from SWVs such as those shown in Figures 2a-d were corrected. In Figure 5, a linear relationship between peak current and square root of frequency was observed as expected from theory (Eq. 3). Using the diffusion coefficient extracted from LSVs in Figure 4, and rearranging Eq. 4, we could then calculate the concentration of CrCl₂. A parity plot relating the calculated concentration to process knowledge concentration is shown on the right in Figure 4. It is interesting to note that when applying this approach across a range of concentrations, the calculated concentration follows the parity line. However, when determining the concentration using Eq. 4, *i.e.*, without using the current multiplier, the concentration plateaus at fairly low values.

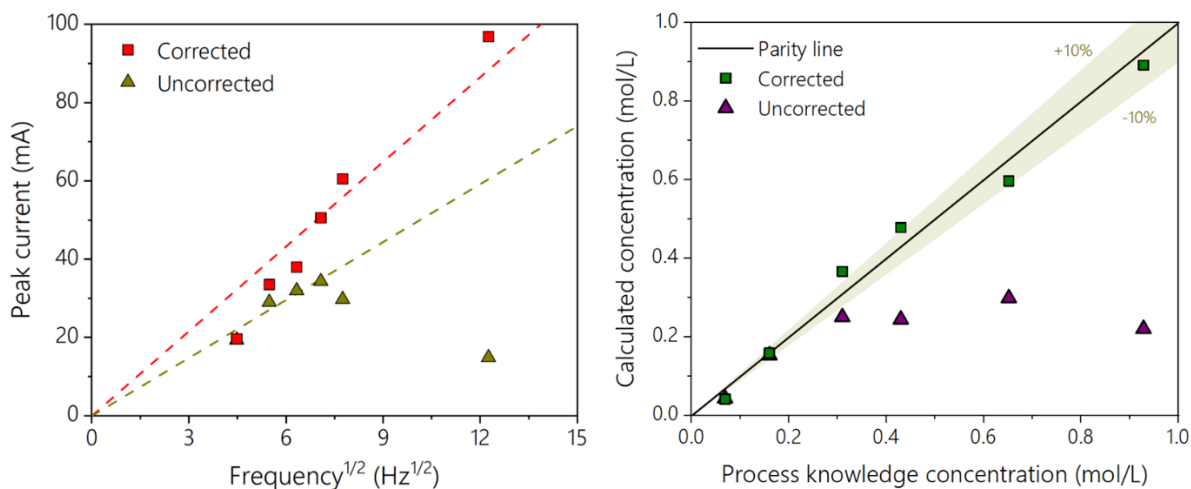


Figure 5. (left) Corrected and uncorrected peak current as a function of square root of frequency and, (right) Parity plot of CrCl₂ concentrations calculated from corrected and uncorrected square wave voltammograms.

2.2.2. Potential Sweep Technique Improvements: Linear Sweep Voltammetry

To further support sensor development in molten salts, we also quantified ohmic resistance distortions in linear sweep voltammetry for soluble-soluble reactions. This has been the topic of numerous studies in literature; however, only a limited number have reported theory-founded methods for post-experiment correction of redox reactions.⁴ Moreover, although this earlier study reported on correction factors for LSVs of electrodeposition reactions, post-experiment correction factors for LSVs of soluble-soluble redox transitions have yet to be reported. As such, the following sections explore the extent of attenuation that uncompensated ohmic resistance poses on soluble-soluble LSVs.

As in the previous section, we used the $\text{Cr}^{2+}/\text{Cr}^{3+}$ redox couple as a model system. Figure 6a shows LSVs collected of CrCl_2 at different scan rates. In Figure 6b, the anodic peak potential increased as a function of scan rate. Additionally, the anodic peak current was a non-linear function of the square root of scan rate as seen in Figure 6c.

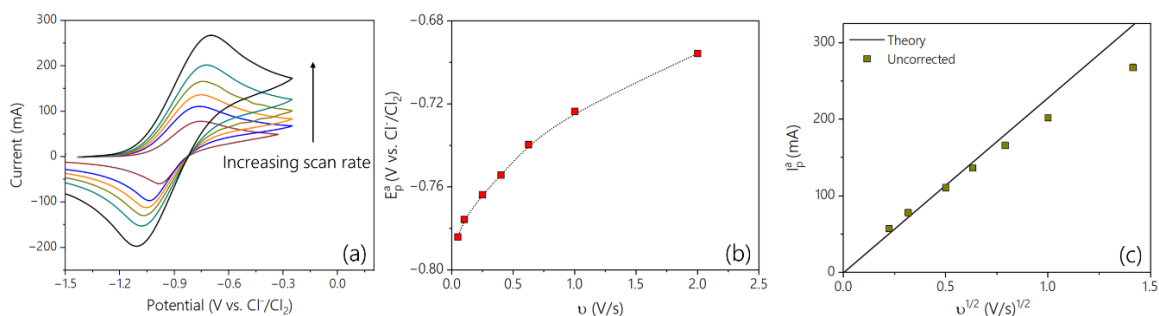


Figure 6. (a) Experimental linear sweep voltammograms collected of CrCl_2 in LiCl-KCl molten salt at various scan rates, (b) variation of anodic peak potential as a function of scan rate, and (c) uncorrected anodic peak current as a function of the square root of scan rate.

To ensure the validity of the simulation prior to introducing uncompensated ohmic resistance, we first simulated LSVs collected at different scan rates under reversible conditions (Figure 7a). Also, we noted the anodic peak potential was clearly independent of scan rate. Recall, from Eq. 6, the Randles-Sevcik equation predicted a linear response of the peak current as a function of the square root of the scan rate. This linearity can be seen in Figure 7b. The dotted line represents a fitted linear regression of the discrete data points shown as red squares. We also calculated the difference between the anodic peak potential and the half-peak potential $E_{p/2}$. Reversible theory dictates that the difference between the two potentials is given by:⁸

$$E_p^a - E_{p/2} = 2.2 \frac{RT}{nF} \quad [5, \text{revisited}]$$

In the case of a one-electron transfer reaction at 450°C , the expected value of $E_p^a - E_{p/2} = 137$ mV. All LSVs shown in Figure 7a agree with the value predicted from Eq. 5 and have values of $E_p^a - E_{p/2} = 138$ mV.

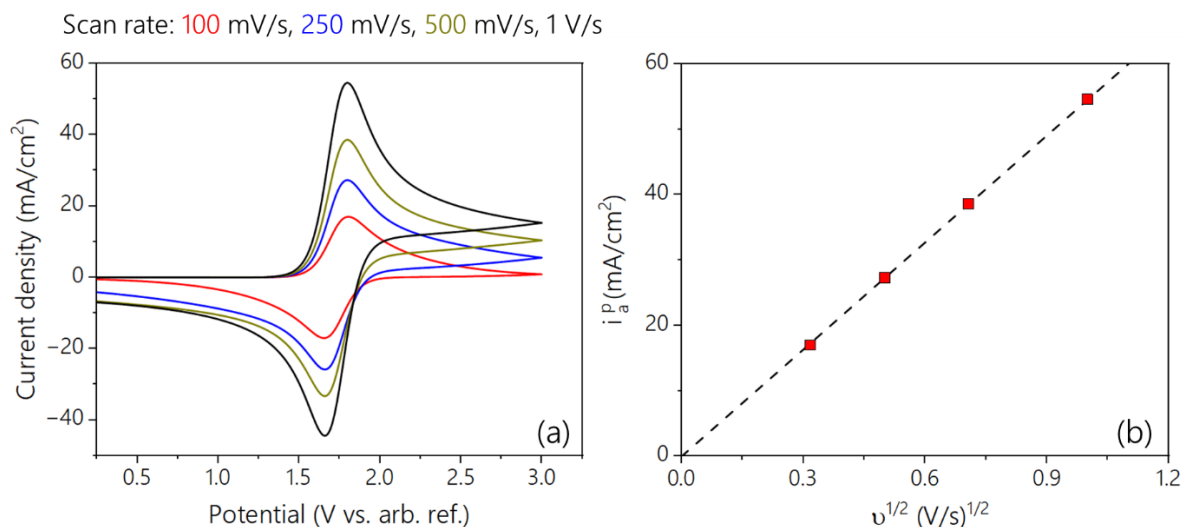


Figure 7. (a) Simulated linear sweep voltammograms in the absence of ohmic resistance, and (b) the corresponding anodic peak current density as a function of scan rate.

Once the validity of the simulation was confirmed, increasing values of uncompensated ohmic resistance were introduced. Representative simulated LSVs with various amounts of uncompensated ohmic resistance are shown in Figure 8a. Note the increasingly attenuated response with increasing iR_Ω : the peak current density was dampened and the difference between the peak potentials increased. As with experiments, we plotted the change in E_p^a as a function of scan rate while maintaining a constant value of R_Ω (seen in Figure 9). Note that a similar non-linear relationship is observed in the case of the simulated E_p^a and experimental E_p^a (Figure 6b).

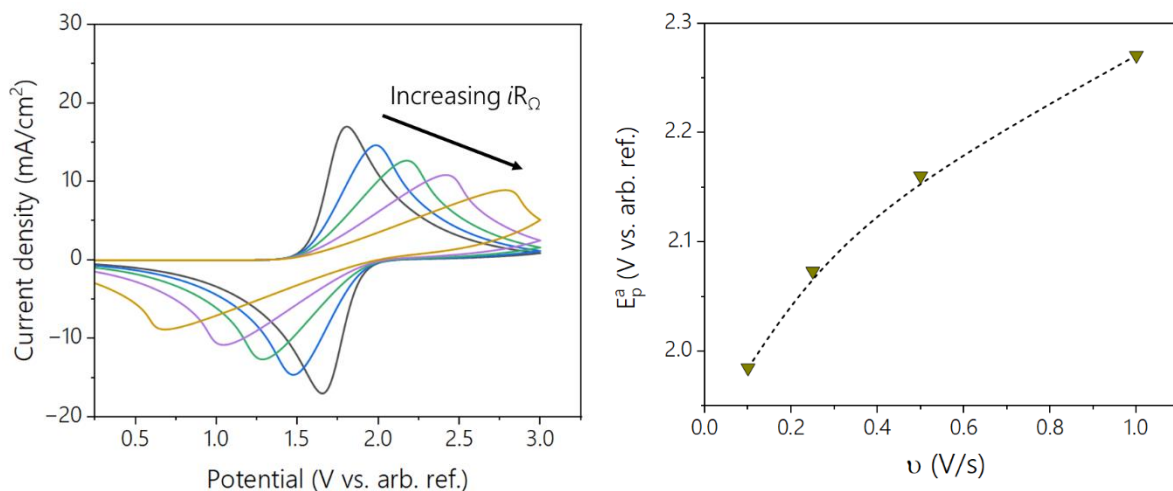


Figure 8. Simulated linear sweep voltammograms experiencing various amounts of uncompensated ohmic resistance.

Figure 9. The shift in the anodic peak potential as a function of scan rate for a fixed value of ohmic resistance.

To precisely quantify this effect, we revisited Eq. 7 from the previous section and applied it to LSVs:

$$CM = \frac{i_p(R_\Omega = 0)}{i_p(R_\Omega > 0)} \quad [7, \text{revisited}]$$

Using this equation, we could relate the current multiplier for a one-electron transfer redox reaction involving a soluble-soluble transition to $E_p^a - E_{p/2}$. Figure 10 shows the specific case of a current multiplier for such a reaction conducted at 450°C. The current multiplier was found to be largely agnostic of scan rate and bulk concentration.

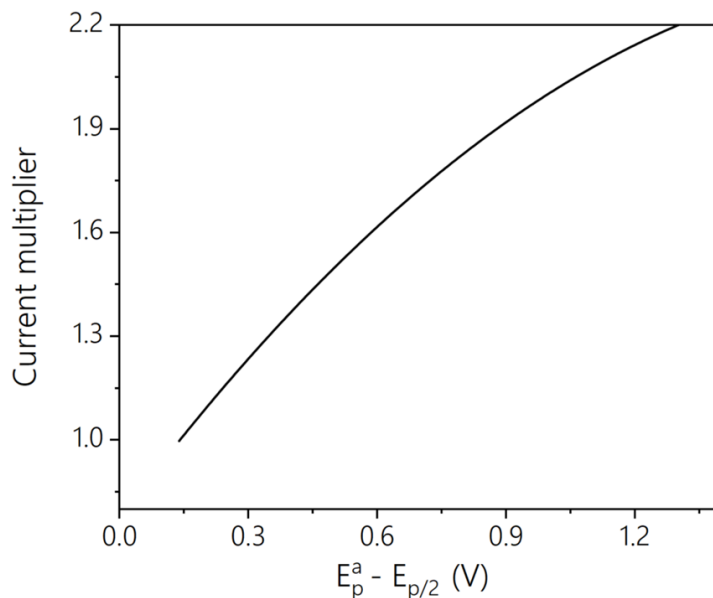


Figure 10. Current multiplier as a function of the difference between anodic peak potential and the half-peak potential.

Using the current multipliers presented in Figure 10, we then corrected experimental data to account for uncompensated ohmic resistance. The corrected peak current is plotted against the square root of scan rate in Figure 11.

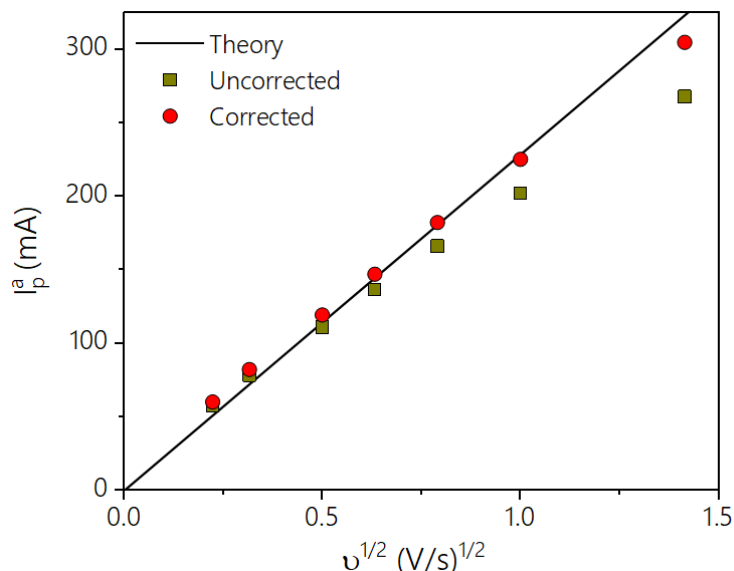


Figure 11. Corrected and uncorrected current compared to predictions from the Randles-Sevcik theoretical equation.

We have noted that, at sufficiently high scan rates, the corrected data still underpredicts the peak current predicted by theory and have attributed this to non-uniform secondary current distribution and possible migration effects. Among the ongoing efforts in FY25 will be to account for current distribution effects in LSVs that are also convoluted by uncompensated ohmic resistance. We expect that by incorporating these effects, a more precise correction factor can be obtained, and more reliable data can be extracted from installed electrochemical sensors.

2.3. Oxide

With the CrCl_2 model system modelled and understood, we could then proceed to characterize oxide species in molten FLiNaK with greater fidelity than had been possible in FY23. First, we identified the electrochemical window by collecting an LSV of pure FLiNaK (*black* curve in Figure 12). The anodic limit corresponded to electrode oxidation and the cathodic limit was identified as potassium electrodeposition. As previously mentioned, at-temperature additions of Li_2O were made to FLiNaK. A representative LSV of one such addition can be seen as the *red* curve in Figure 12. Here again, we observed potassium electrodeposition on the cathodic limit of the LSV. However, an increase in current at potentials more anodic than electrode oxidation was observed and attributed to oxygen evolution. This can be further confirmed by the appearance of noisy, sporadic spikes in current that is characteristic of gas evolution reactions.

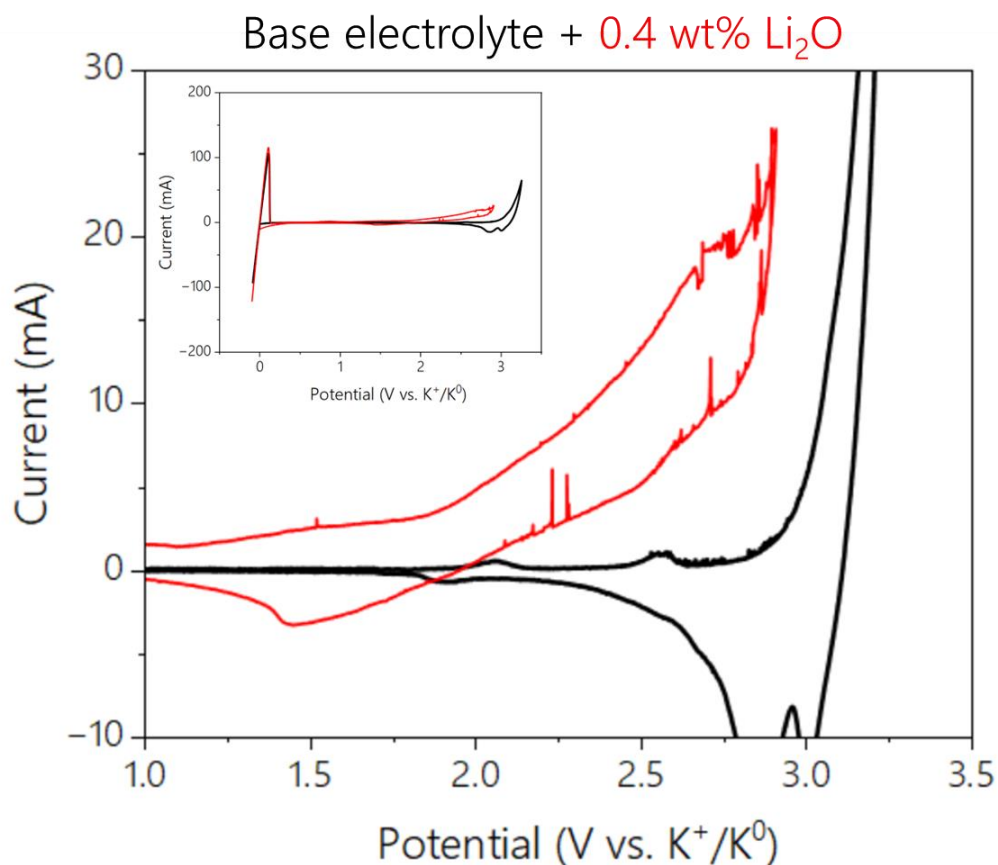


Figure 12. Linear sweep voltammogram of (*black*) pure FLiNaK, and (*red*) 0.4 wt% Li₂O.

To study this system, we again used the simplified electrode array system described previously.¹³ In FY23, we reported on current multipliers for 4-electron transfer reactions.⁵ As such, we limit the discussion in this section to corrected peak current values only. Figure 13a-d shows SWVs collected across a range of frequencies. Using the current multipliers reported in FY23, we could then correct the values of the peak currents versus the square root of frequency at two different heights, as shown in Figure 13e.

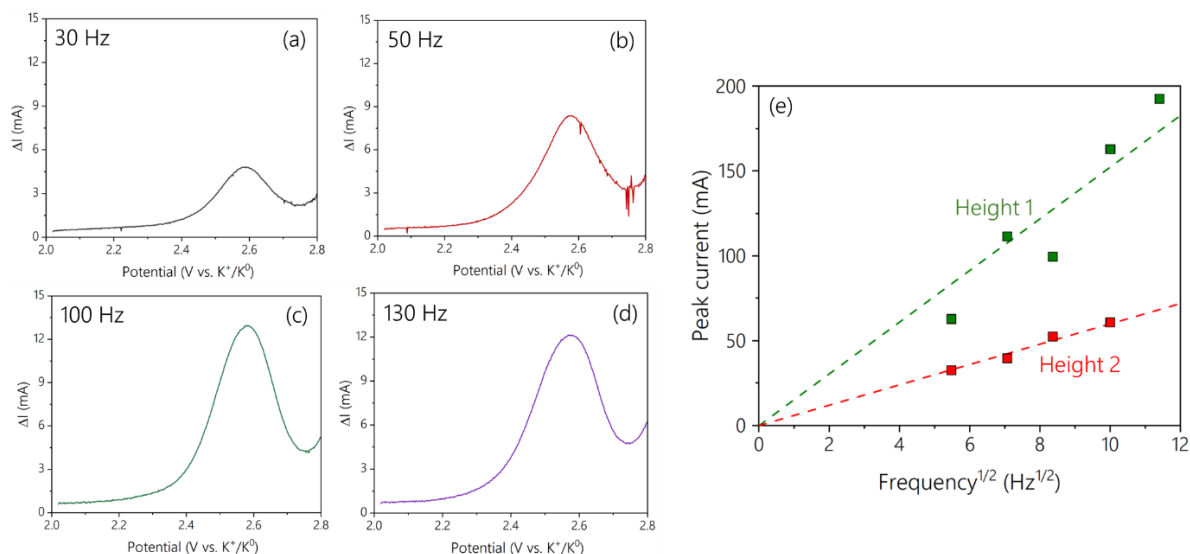


Figure 13. (a-d) Square wave voltammograms of the $2O_2^- \rightarrow O_2 + 4e^-$ redox reaction collected at various frequencies, and (e) the relationship between the corrected peak current and square root of frequency for two different electrode immersion depths.

Using information from Figure 13e, we could then determine the electrode area and ultimately the diffusion coefficient of O_2^- under different conditions. This approach was taken for SWVs collected at different temperatures, namely 550°C, 600°C, 650°C and 700°C. In well-behaved systems, the diffusion coefficient varies with temperature according to the Arrhenius equation:

$$\log(D) \propto \frac{1}{T} \quad [9]$$

When this approach was taken, the corrected (*red circles*) values of O_2^- diffusion coefficients varied linearly with the inverse of temperature as shown in Figure 14. As a reference point, uncorrected (*blue triangles*) values are also shown to further highlight the unpredictability of raw data without proper correction for uncompensated resistance. These corrected diffusion coefficient values form the basis of oxide measurements as the sensors are deployed in additional FLiNaK loops and systems in the future.

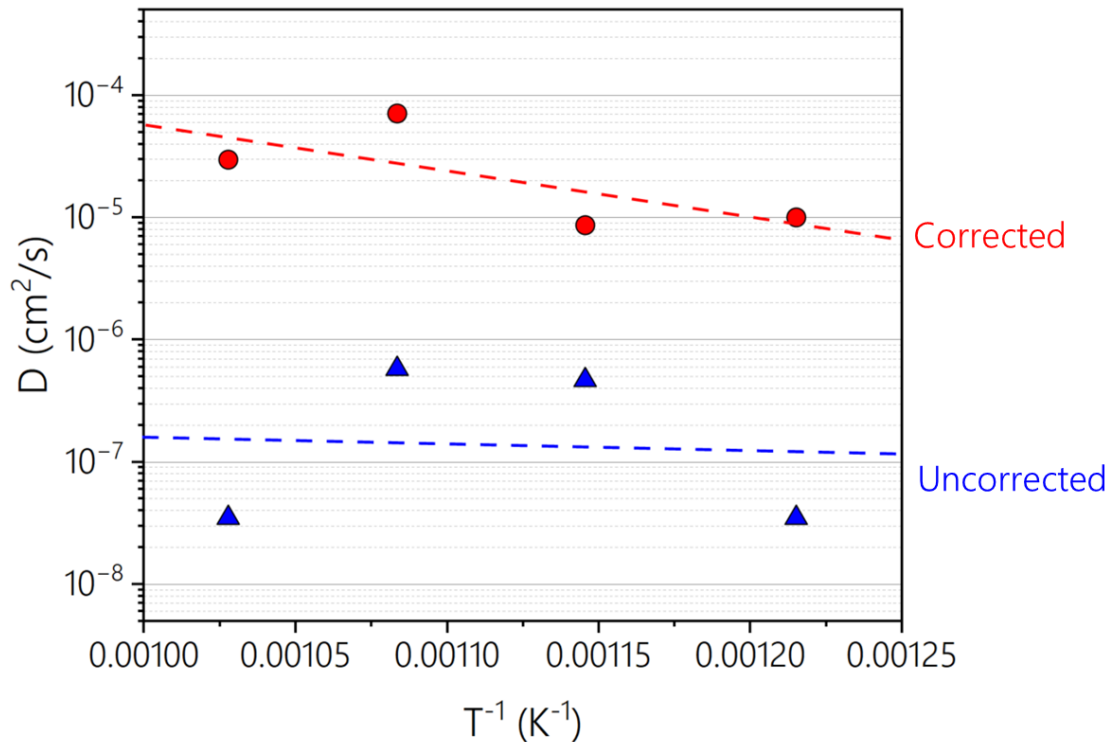


Figure 14. (red circles) Corrected and (blue triangles) uncorrected diffusion coefficients as a function of inverse temperature.

3. Sensor Deployment Results

In FY24, the FASTR loop at Oak Ridge National Laboratory (ORNL) was brought back into service to support MSR-relevant technology demonstrations. Initial resumption of operations for FASTR lasted for approximately 70 hours using molten $\text{MgCl}_2\text{-KCl-NaCl}$. Electrochemical sensors from Argonne were deployed to monitor the salt's status in the pump vessel during these operations. Photos of this sensor are shown in Figure 15.¹⁴ The sensor featured multielectrode arrays connected to a customized multiplexer for accurately obtaining the surface area of the electrodes. Figure 16 shows a typical linear sweep voltammogram measured on one of the sensor's electrodes. Each measurement typically consisted of at least two scans with one scan towards the reducing potential to obtain the salt redox potential relative to the reduction potential of Mg^{2+} and the other scan towards the oxidizing side to clean the working electrode and ensure the long-duration repeatability of the measurements. In addition, the state of the electrodes was also assessed using electrochemical impedance spectroscopy (EIS). Repeatability of the EIS results were used to inform the efficacy of electrode cleaning procedures and examine other aspect of the evolution of the salt chemistry. During the operation of the FASTR loop, the salt redox potential and resistance was periodically monitored, as shown in Figure 17 and Figure 18. It was observed that the initial salt redox potential was low (approximately 0.4V vs. Mg/Mg^{2+}), which indicated a minimal presence of impurities such as O^{2-} , OH^- and other metal cations. This low potential was likely due to the presence of excess Mg metal in the salt and is consistent with earlier measurements from the purification vessel.¹⁴ The salt redox potential modestly increased throughout operations but remained at a relatively low level (approximately 0.6V vs. Mg/Mg^{2+}). The salt resistance remained near constant with small variation over time which could be a result of temperature variations.¹⁵ Overall, the results indicated proper operations of the sensor within the FASTR environment.



Figure 15. Photos of the electrochemical sensor assembly (*left*) before deployment in FASTR loop, and (*right*) after operation in FASTR.

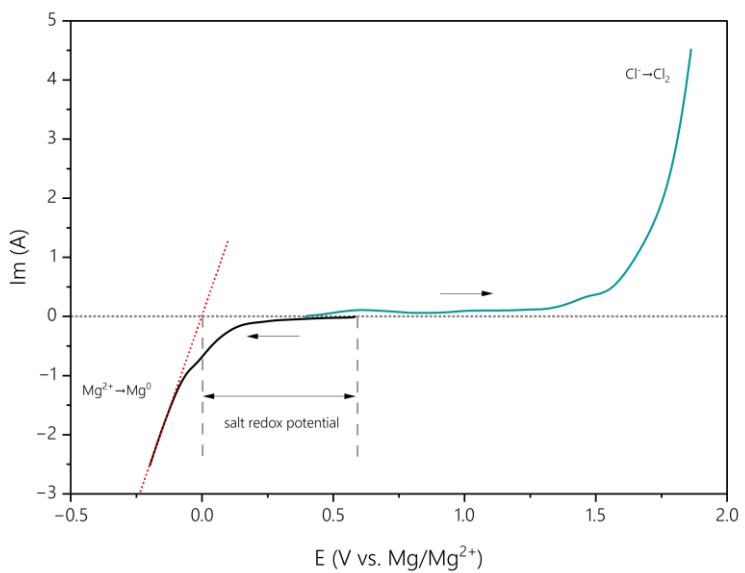


Figure 16. Typical linear sweep voltammogram of $MgCl_2$ -KCl-NaCl.

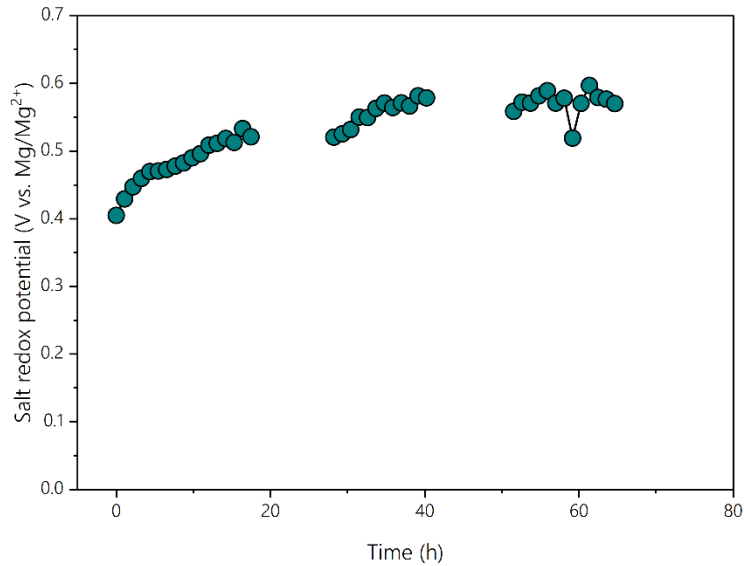


Figure 17. The salt redox potential variation over time.

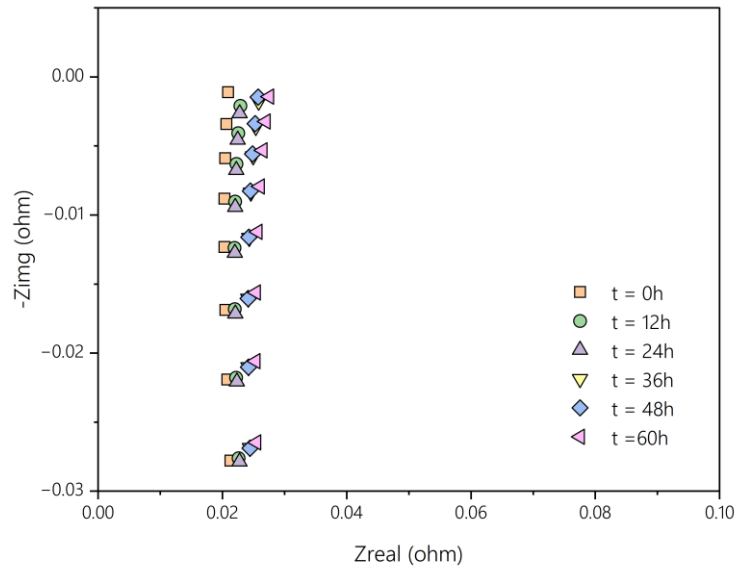


Figure 18. Nyquist plots of EIS measurement results during FASTR operation.

The sensor results were also able to assess the chemical state of the loop's salt with respect to its optimal operating range. These conditions are described by the operational envelope. To define the operational envelope for the FASTR loop, *i.e.*, the ideal salt redox potential and O^{2-} activity (concentration) ranges that minimize the corrosion of structural materials, the deposition of reactive metals, and the formation of insoluble oxides in the molten $MgCl_2$ - KCl - $NaCl$ environment, we constructed a Littlewood diagram for Cr and Mg species in this salt system as shown in Figure 19.¹⁶ In the diagram, the x -axis is pO^{2-} , the negative logarithm of O^{2-} activity which reversely indicates the O^{2-} activity, while the y -axis is the system redox potential against the redox potential of Mg/Mg^{2+} . The horizontal lines represent reactions with oxidation state change that are independent of O^{2-} activities, such as Reactions 10-13 listed below; the vertical lines represent the equilibrium O_2 activity for reactions without oxidation state changes like

Reactions 14 and 15; the sloped lines represent reactions with oxidation state changes that are dependent on O^{2-} activities, such as Reactions 16 and 17. The position of the lines is determined with the Gibbs free energy of formation for MgO, MgCl₂, Cr₂O₃, CrCl₂ and CrCl₃ calculated using HSC9[®] (listed in Table 1). These lines segregated the predominance diagram into four regions with the bottom region as the pure metal region, the middle-left region as the metal oxide region, the middle-right region as the metal chloride region, and the top region as the chlorine evolution region.

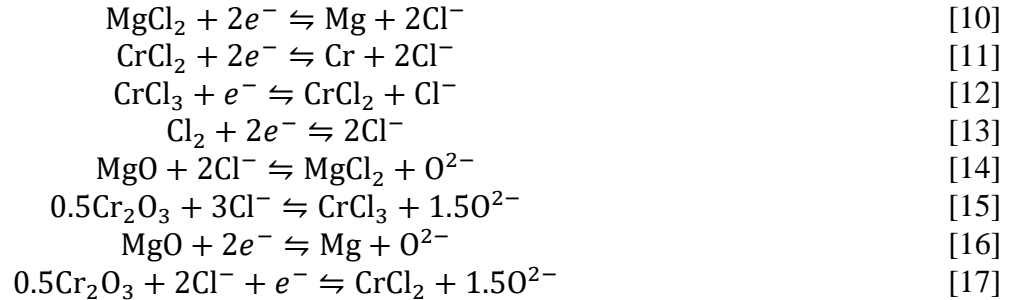


Table 1. Gibbs free energy of formation at 823K.

Species	G _f [°] (kJ)
MgCl ₂	-509.07
MgO	-512.98
CrCl ₂	-285.51
CrCl ₃	-356.68
Cr ₂ O ₃	-920.13

As seen in the diagram, the salt potential during FASTR operations (0.4V – 0.6V vs. Mg/Mg²⁺) was well below the threshold for Cr²⁺ formation in the salt. Consequently, no Cr²⁺ impurities were detected. The salt potential and resistance gradually increased over the course of the test indicating the ingress of O₂ in the melt. As oxide measurements were not taken voltammetrically during operations and since the O₂ content of the cover gas was unmeasured, we could not estimate the O²⁻ activity in the salt during FASTR operations. As such, the operational state is notionally shown to extend across the entire range of pO²⁻ values. If additional opportunities for measurements within FASTR become available, the techniques developed in Section 2 will be used to better define the precise pO²⁻ of the dissolved oxide present in the loop. According to the diagram, maintaining the pO²⁻ between 6 to 10 and the salt potential between 0.2 and 0.8V vs. Mg/Mg²⁺ can minimize both the corrosion of structural materials and the formation of solid oxide particles. This defines the operational envelope for the FASTR loop. To maintain the loop within this envelope, methods such as periodic additions of Mg metal and/or sparging with anhydrous HCl can be applied.

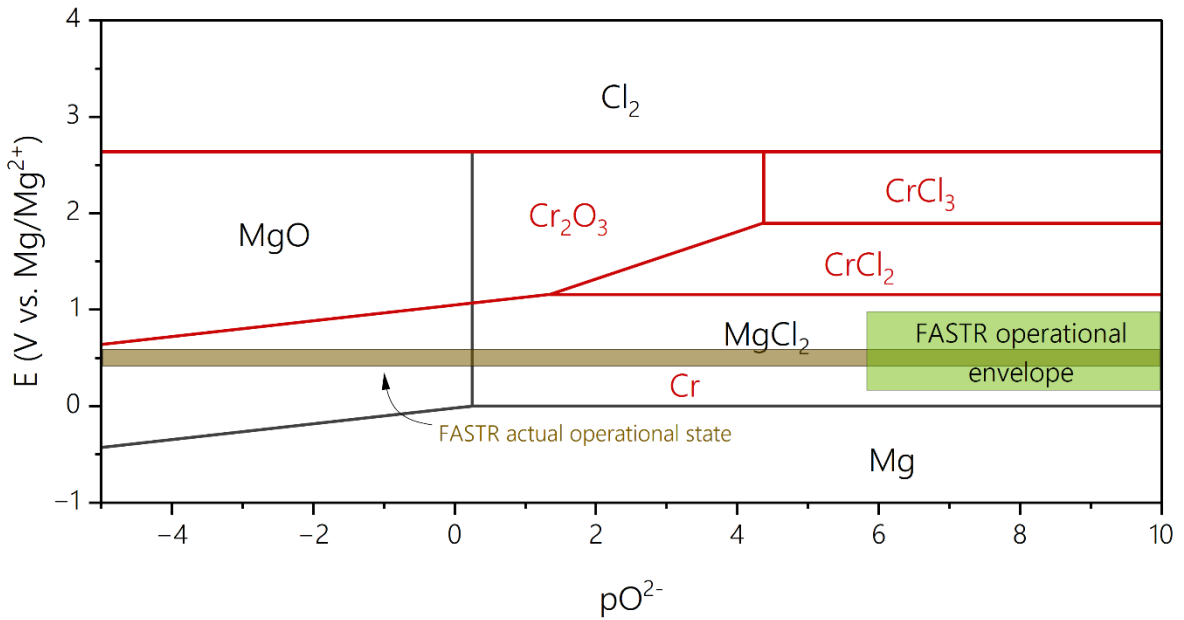


Figure 19. Littlewood diagram of Cr and Mg species in molten $MgCl_2$ -KCl-NaCl with operational status and ideal operational envelope for FASTR.

4. ANL Actinide Loop and Corrosion Control System Design

4.1. Actinide Loop Design

During mid-FY24, the design and procurement of an actinide molten salt loop was initiated at Argonne. The loop's purpose is to enable the development and testing of molten salt reactor technologies using realistic salt compositions. The loop will be suitable for installation into a radiological glovebox, thereby enabling rapid integration of new components and changeover of salts. Planned testing capabilities include long-duration operations relevant to corrosion and salt chemistry control.

To achieve these goals, a suitable radiological glovebox containing furnace wells was identified for installation of the loop. Figure 20 shows the glovebox exterior and furnace well positioned beneath the box. The furnace well is connected to the glovebox by a flange with O-ring seals. The geometric requirements of the well and temperature limits of the flange have driven the design of the molten salt pump that forms the basis of the loop.



Figure 20. (*left*) Radiological glovebox where the pumped actinide loop will be installed, and (*right*) typical furnace well located under glovebox.

The final pump design that meets the requirements for glovebox installation is shown in Figure 21. The unit is a miniature pump from High Temperature System Designs, LLC that has a substantially modified heat shield pack, upper plate, and other features to enable installation in our testing environment. The pump is capable of being disassembled into three sections to allow piecewise insertion through the glovebox transfer lock.

The top mounting plate includes two 1” ports for the pump discharge and return, along with four 0.75” ports for the installation of sensors, corrosion control, sampling, and other systems. An identical pump has been purchased for molten salt sampler activities being conducted under DOE NE’s MPACT program (Work Package FT-24AN04010305), but the loop configuration is completely different. The pump is inserted down into the furnace well where it is submerged in the salt. The reservoir within the furnace well is completely open to the glovebox pressure, which means that the system is not comprised of any pressure vessels that require ASME BPV code compliance. The loop’s process piping, however, is covered by ASME B31.3.

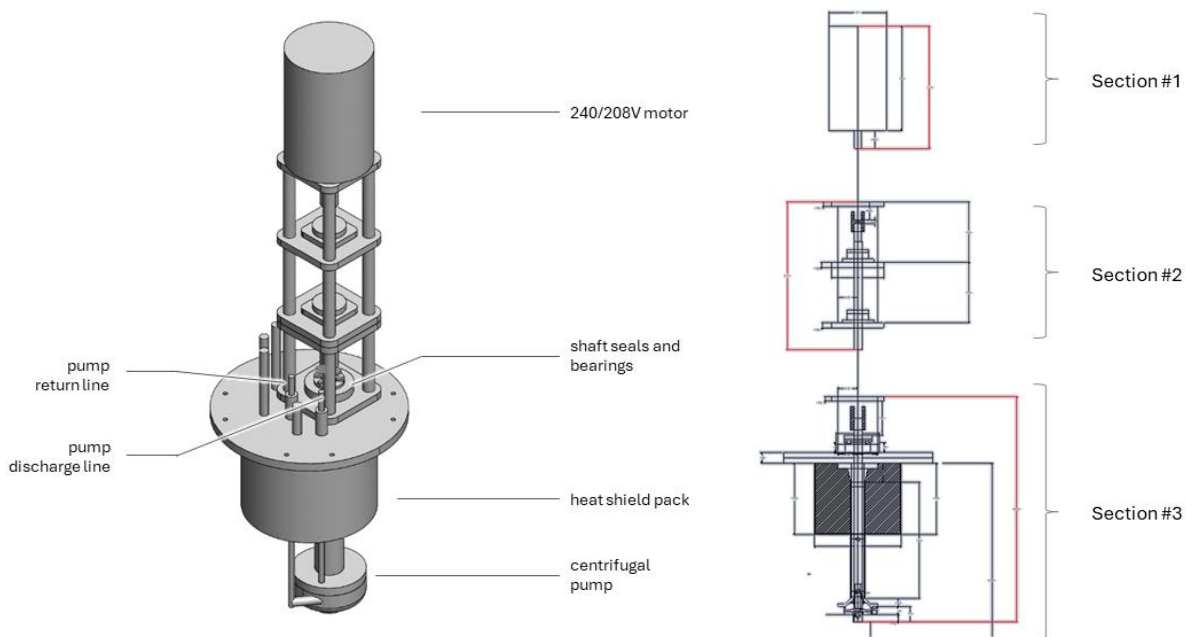


Figure 21. (left) Rendering of molten salt pump, and (right) pump sections enabling insertion through transfer lock.

A rendering of the loop design is shown in Figure 22. The system supports multiple configurations as components can be easily swapped out using the Swagelok compression fitting connections. Use of Swagelok fittings for molten salt flow loops located external to a glovebox is typically not advisable due to the likelihood of small leaks, particularly after multiple connections and disconnections. However, the small salt vapor leaks that may occur due to these fittings are acceptable in the glovebox as the low- O_2 and low- H_2O atmosphere will not initiate any aggressive corrosion.

The loop also includes a salt-to-argon heat exchanger to achieve desired temperature gradients across the loop. The maximum achievable temperature difference is a function of flow rate and of the glovebox heat rejection capabilities. Two auxiliary glovebox chiller systems are currently in place, along with flange cooling to support loop operations. A third chiller system may be added if needed to reject additional heat and achieve the targeted temperature range.

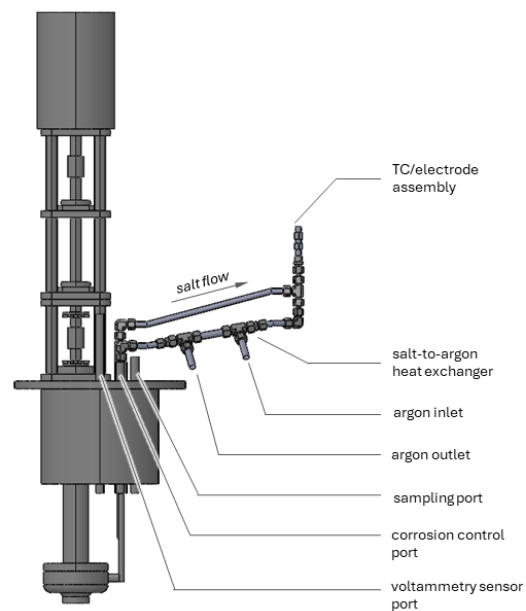


Figure 22. Annotated rendering of actinide loop.

Procurement of pump and loop components is currently underway. The pump is expected to arrive by October 2024, after which it will undergo water testing. Overall, the glovebox provides several advantages that have so far allowed this system to be assembled quickly and economically. For example, the ability to operate the system without coded pressure vessels allows us to use easily available materials such as 316L stainless steel for the salt-wetted components and containers. The glovebox also offers advantages for safe and flexible operations – if needed, parts and components can be swapped out easily without risking radiological contamination or ingress of corrosion-inducing impurities into the system.

4.2. Corrosion Control System

During FY24, we also finalized the design of the corrosion control system that will be used on the actinide loop. The design of the system is based on earlier systems developed at Argonne but needed updates due to the planned use with an actinide-bearing salt. Our previous control systems had targeted deployment to ORNL’s Liquid Salt Test Loop (LSTL), which has a FLiNaK salt, but circumstances prevented operations of those systems there.

Transitioning to the actinide loop required changes to the corrosion control agents, but the overall approach is identical: controlling the salt chemistry to be in the appropriate window where oxidation of metals from the structural alloys is minimized while simultaneously minimizing deposition into the structure. Accomplishing this requires careful control of the salt redox potential to maintain the system in its appropriate operational envelope.

The system that we have designed to achieve this is shown in Figure 23. The apparatus includes a liquid metal alloy pool that can contain reactive metals at various activity levels to maintain the salt in the targeted range. The system has been designed to be installed via one of the 0.75” ports on the actinide loop’s top plate. Insulated electrodes placed the support tube allows for selective connection of the liquid metal pool to the loop’s structural metals. Under normal operations the pool will be connected by zero-resistance amperometry to the salt structure, although disconnection will be performed if dictated by salt conditions. Additions of reactive metals, including uranium, into the pool will be possible by detaching the electrode assembly from the support tube.

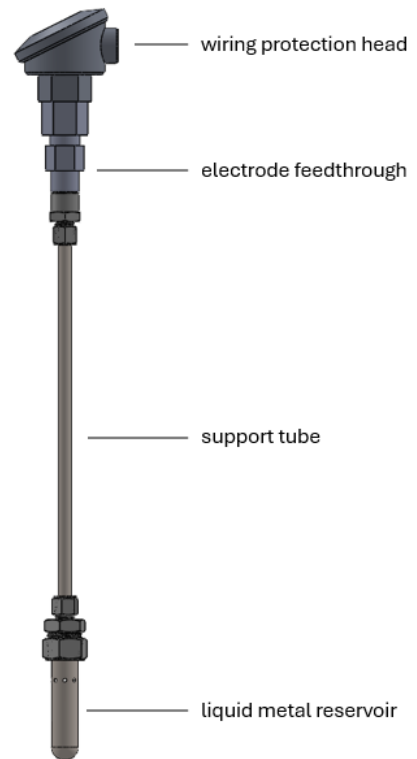


Figure 23. Rendering of corrosion control assembly

Procurement of parts for the corrosion control system is underway, and acquisition of uranium metal for use as a reducing agent has also been initiated. Argonne’s ILEX software will be used to automate operations of the corrosion monitoring system.¹⁷

5. Conclusions and future work

Our work in FY24 focused on developing new tools and approaches to support the monitoring and operation of MSR-relevant molten salt systems. This included the creation of improved electroanalytical techniques leveraging digital simulations to enable the measurement of dissolved impurities such as Cr^{2+} and O^{2-} across complete ranges of interest, along with the deployment of sensors to monitor the chemical state of salt within the FASTR loop at ORNL. Additionally, we finalized the design of our loop-deployable corrosion control system and developed a flow loop to provide a platform for testing these chemistry and corrosion control capabilities in actinide-bearing fuel salts.

Moving forward to FY25, we plan to install the actinide loop into our radiological glovebox and synthesize salt for its operations. The corrosion monitoring system and associated voltammetry sensors will also be installed into the system, with operations expected by the end of the fiscal year. Beyond this, we will continue to deploy and operate sensors to support the monitoring of additional loops across the national laboratory complex in support of the Department of Energy Office of Nuclear Energy's MSR Campaign. In total, the activities this year and next year will serve to create new technologies and approaches to increase the maturity, safety, and efficiency of molten salt reactor operations.

6. References

1. C. F. Baes, Jr., *J. Nucl. Mater.*, **51**, 149 (1974).
2. E. L. Compere, S. S. Kirslis, E. G. Bohlmann, F. F. Blankenship, W. R. Grimes, ORNL-4865 (1975).
3. R. C. Robertson, ORNL-TM-728 (1965).
4. N. C. Hoyt, J. L. Willit, and M. A. Williamson, *J. Electrochem. Soc.*, **164**(2), H134 (2017).
5. N. A. Shaheen, J. Guo, and N. C. Hoyt, ANL/CFCT-23/29 (2023).
6. E. P. Parry and R. A. Osteryoung, *Anal. Chem.*, **37**(13), 1635 (1965).
7. L. Ramaley and M. S. Krause, Jr., *Anal. Chem.*, **41**(11), 1363 (1969).
8. A. J. Bard and L. R. Faulkner, *Electrochemical Methods Fundamentals and Applications* (John Wiley & Sons, New York) (2001).
9. Ševčík, *Collect. Czech. Chem. Commun.*, **13**, 349 (1948).
10. J. E. B. Randles, *Trans. Faraday Soc.*, **44**, 327 (1948).
11. F. Lantelme, K. Benslimane, and M. Chemla, *J. Electroanal. Chem.*, **337**, 325 (1992).
12. V. Mirčeski and M. Lovrić, *J. Electroanal. Chem.*, **497**, 114 (2001).
13. J. Guo, N. Hoyt, and M. Williamson, *J. Electroanal. Chem.*, **884**, 115064 (2021).
14. K. R. Robb, S. Baird, J. Massengale, N. Hoyt, J. Guo, and C. Moore, ORNL/TM-2022-2554.
15. N. A. Shaheen, J. Guo, and N. C. Hoyt, ANL/CFCT-23/29 (2023).
16. R. Littlewood, *J. Electrochem. Soc.*, **109**(6), 525 (1962).
17. C. E. Moore, W. H. Doniger, and N. C. Hoyt, ANL/CFCT-23/28 (2023).



Chemical and Fuel Cycle Technologies Division

Argonne National Laboratory
9700 South Cass Avenue, Bldg. 205
Argonne, IL 60439

www.anl.gov



Argonne National Laboratory is a U.S. Department of Energy
laboratory managed by UChicago Argonne, LLC